Measuring the intralaminar crack resistance curve of fibre reinforced composites at extreme temperatures

Measuring the intralaminar crack resistance curve of fibre reinforced composites at extreme temperatures

R. F. Pinto[a,b], G. Catalanotti[a,c], P. P. Camanho[a,b,*]

[a] *INEGI, Instituto de Ciência e Inovação em Engenharia Mecânica e Engenharia Industrial, Rua Dr. Roberto Frias, Campus da FEUP, 400 4200-465 Porto, Portugal*
[b] *DEMec, Faculdade de Engenharia, Universidade do Porto, Rua Dr. Roberto Frias, 4200-465 Porto, Portugal*
[c] *School of Mechanical and Aerospace Engineering, Queen's University Belfast, Belfast BT9 5AH, UK*

Abstract

This work focuses on the development of methods to measure the intralaminar fracture toughness of IM7/8552 CFRP at extreme temperatures. The size effect law of scaled double-edge-notched (DEN) specimens is used to obtain the crack resistance curves associated with longitudinal failure of polymer composites. The compressive and tensile crack resistance curves are determined and compared to those measured at room temperature. Scanning electron microscopy is used to analyse the fracture surface of tensile DEN specimens as a means to understand the damage mechanisms involved and their dependence on temperature variations. It is shown that the methods proposed enable the measurement of the crack resistance curve under different environment conditions. The results obtained can be used in analytical models to evaluate the integrity of composite structures at extreme temperatures.

Keywords: *Fibre reinforced materials, Fracture mechanics, R-curve, Intralaminar fracture toughness, Size effect, Temperature, Material characterization, Elastic properties, Scanning electron microscopy*

*Corresponding author
Email address: pcamanho@fe.up.pt (P. P. Camanho)

1. Introduction

Recent analysis models that predict fracture of composite structures require the values of the fracture toughness associated with different failure modes [1, 2, 3, 4]. In particular, the intralaminar fracture toughness is required not only for material screening and characterization but also for identifying the softening constitutive relation that simulates longitudinal tensile and compressive failure [1, 5].

While recent work has been performed on the measurement of crack resistance curves (R-curves) associated with longitudinal fracture at room temperatures [6, 7], there is no information on the effects of extreme temperatures on the corresponding R-curves. Taking into account that the structural integrity must be preserved under different working scenarios and environments, in particular at extreme temperatures, the objective of this paper is to study how extreme temperatures affect the crack resistance curve of polymer composites that fail under longitudinal tension and compression. Taking the commercial aerospace industry as an example, composite materials need to fulfil their structural requirements at room temperature, at flight cruise altitude where temperatures can be lower than $-50°C$, while also reaching high temperatures at the vicinity of the engine and engine fluid flow systems.

Temperature does not affect the carbon fibre properties but has influence on the polymer matrix and on the fibre-matrix interface [8], thus changing the mechanical response of the composite system. Due to the complex behaviour of composite materials under different thermal conditions, the mechanical response under temperature variations is difficult to predict.

The dependence of composite materials modulus and stiffness on temperature is well known and documented [9, 10, 11]. As temperature increases, the polymer Young's modulus suffers a transition from 'glass-like' to 'rubber-like' and the abrupt drop in modulus takes place at the glass transition temperature, denoted as T_g. The strength of composite materials is directly connected to the intrinsic properties of its constituents, even if fibres are almost tempera-

ture insensitive the overall mechanical properties of the composite are affected due to the matrix/fibre interface property changes. In fact, as the temperature increases, the matrix stiffness decreases, which causes a decrease of the laminate's strength [12, 13, 14]. A study conducted by Whitley and Gates [15] has shown that for cryogenic temperatures the shear modulus and strength increase as temperature decreases.

Kim et al. [16, 17] investigated the effects of temperature on the mode I and mode II interlaminar fracture of CFRP. As temperature increases, $\mathcal{G}_{IC}$ decreases slightly for the unidirectional laminate $[0]_{24}$ but increases for the other two laminates with different ply orientations [16]. However, as temperature increases, $\mathcal{G}_{IIC}$ decreases for all three laminates considered.

Despite the aforementioned work, no relevant work has been performed to measure the R-curve at extreme temperatures. Commonly used procedures to measure the tensile fracture toughness and tensile crack resistance curve (R-curve) use approaches developed for metals such as the compact tension (CT) and the compact compression (CC) test specimens [6, 7]. The use of these specimens together with proper reduction methods on brittle materials provides accurate results [7, 18]. However, with the introduction of new tougher resins, higher loads are required for crack propagation, which may lead to buckling at the un-notched end of the test specimen [18].

Recent work provides reliable test methods to accurately obtain the R-curve associated with the tensile and compressive longitudinal failure [19, 20]. In the last case, failure corresponds to the formation and propagation of kink bands, which brings new challenges to the measurement of the compressive fracture toughness and crack resistance curve [21, 22].

The present work relies on the size-effect method initially proposed by Bažant [23] based on the relation of the size effect law with the R-curve. This method was extended by Catalanotti et al. [19, 20, 24] to measure the intralaminar R-curves in fibre reinforced composites and is used to experimentally determine the R-curve of IM7/8552 CFRP at extreme temperatures. The results are then compared with the tensile and compressive R-curve of the same material mea-

sured at room temperature following the same method [19, 20]. Since these new methods do not require any form of tracking of the crack size during testing, they can be used in working conditions under several extreme environment scenarios, where some type of enclosure for the specimens is involved. Applying these new approaches it is possible to achieve accurate measurements with near zero visibility to the specimen undergoing the test.

2. Materials and methods

2.1. Analytical model

For a two-dimensional orthotropic body with x and y as the preferred axes of the material, the energy release rate (ERR) in mode I necessary for crack propagation in the x-direction can be described using the following equation [25]:

$$\mathcal{G}_I = \frac{1}{\acute{E}}\mathcal{K}_I^2 \tag{1}$$

where $\mathcal{K}_I$ is the stress intensity factor and $\acute{E}$ is the equivalent modulus defined as:

$$\acute{E} = \left(s_{11}s_{22}\frac{1+\rho}{2}\right)^{-1/2}\lambda^{1/4} \tag{2}$$

where s_{lm} are the components of the compliance matrix in the $x-y$ coordinate system, λ and ρ are two dimensionless elastic parameters that take into account the anisotropy of the material and are defined as [25]:

$$\lambda = \frac{s_{11}}{s_{22}}, \qquad \rho = \frac{2s_{12}+s_{66}}{2\sqrt{s_{11}s_{22}}} \tag{3}$$

Note that the compliances are functions of the temperature and therefore λ and ρ vary with the applied temperature.

The stress intensity factor, $\mathcal{K}_I$ in Eq. (1) is a function of ρ, of the remote stress σ and of the geometry of the specimen [25, 26] and it reads:

$$\mathcal{K}_I = \sigma\sqrt{w}k(\alpha,\rho,\lambda) \tag{4}$$

where $\alpha = a/w$ is the shape-parameters and k is the correction factor that depends on the geometry and orthotropy of the material. Replacing (4) in equation (1), $\mathcal{G}_I$ yields:

$$\mathcal{G}_I = \frac{1}{\acute{E}} w\sigma^2 k^2 = \frac{1}{4w\acute{E}} \left(\frac{Pk}{t}\right)^2 \tag{5}$$

where t is the thickness of the specimen and P is the applied load. Assuming that k is an increasing function of the crack length (the specimen has a positive geometry), the size effect can be used to measure the fracture toughness of the material [27] using (5):

$$\mathcal{G}_I(\Delta a) = \frac{P^2}{4wt^2\acute{E}} k^2 \left(\alpha_0 + \frac{\Delta a}{w}, \rho, \lambda\right) \tag{6}$$

where $\alpha_0 = a_0/w$.

For different geometries w_n, the crack driving-force curves $\mathcal{G}_I$ corresponding to the peak loads P_{un} are tangent to the R-curve. This is the basis of the method used to measure the R-curve $\mathcal{R}$. The peak load P_u and thus the ultimate remote stress $\sigma_u = P_u/(2wt)$ can be obtained using Eq. (7):

$$\begin{cases} \mathcal{G}_I(\Delta a) = \mathcal{R}(\Delta a) \\ \frac{\partial \mathcal{G}_I(\Delta a)}{\partial \Delta a} = \frac{\partial \mathcal{R}(\Delta a)}{\partial \Delta a} \end{cases} \tag{7}$$

Assuming that the size effect law is known $\sigma_u = \sigma_u(w)$ and replacing Eq. (5) in the first of Eq. (7) results in:

$$\mathcal{R}(\Delta a) = \frac{1}{\acute{E}} w\sigma_u^2 k^2 \tag{8}$$

Eq. (8) is valid for all values of w. Differentiating Eq. (8) [27] with respect to w, assuming that geometrically similar specimens are tested (α_0 is independent of the width, w) and knowing that the R-curve does not depend on w ($\frac{\partial \mathcal{R}}{\partial w} = 0$), results in:

$$\frac{\partial}{\partial w}(w\sigma_u^2 k^2) = 0 \tag{9}$$

this equation can be solved for $w = w(\Delta a)$ which when replaced in (8) yields the R-curve, $\mathcal{R}(\Delta a)$.

According to Bažant and Planas [27], the size effect law should be determined testing geometrically identical samples and applying one of the three types of fitting approaches: (i) the bilogarithmic regression, (ii) the linear regression I or (iii) the linear regression II. Table 1 shows the formulas for the calculation of the length of the fracture zone l_{fpz} and for the fracture toughness $\mathcal{R}_{SS}$ for each regression fit normally used where $k_0 = k|_{\alpha=\alpha_0}$ and $\acute{k}_0 = \partial k/\partial\alpha|_{\alpha=\alpha 0}$.

[Table 1 about here.]

Figure 1 shows the geometry of a double edge notched (DEN) compression and tension specimen. The width of the specimens is $2w$ and the initial crack length is a_0. The length of the compression specimen is $3w$ and the length of the tension specimen is $2l$.

[Figure 1 about here.]

A calculation of the correction factor is presented in [19] and [20] for both the compressive and tensile specimen.

2.2. Experimental testing

All tests were performed in an Instron 4208 testing machine equipped with a 100 kN load cell and fitted with a Instron environmental chamber model 3119-007. For the high temperature tests, the two electrical resistances within the chamber were used to achieve the required temperature of 100 °C. For the low temperature, liquid nitrogen (N_2) was injected inside the chamber until the pre-set temperature value of -50 °C was achieved. This process is controlled by an automatic solenoid valve that continuously manages the inflow of the cooling fluid.

To secure the tensile specimens, an extension was manufactured and mounted between the load cell and the upper grip. Such extension allows enough clearance for the vertical movement and also makes possible to use 250 mm long

specimens whilst having the specimen subjected to the desired temperature. For the compressive specimens, a lower extension adapter was designed and manufactured to increase the height of the bottom section of the compression rig component. This adapter is composed of a self alignment mechanism that sits on top of the extension, which in turn bolts directly into the Instron 4208 base table. The self-alignment mechanism consists of two parts connected by a spherical joint, the top part is equipped with a tungsten-carbide insert in order to prevent indentation when in contact with the specimen. The bottom part of this assembly is fixed to the bottom extension, which is then bolted to the Instron 4208 testing machine (Figure 2).

[Figure 2 about here.]

For all tests, the specimens were placed inside the chamber and the chamber temperature control was set to the desired temperature. After the chamber thermocouple reading output reached the desired temperature value, the specimen was allowed to stabilize for a period of no less than 30 minutes prior to testing. Compensation for material shrinkage (-50 °C) and/or swelling (100 °C) during stabilization was performed manually using the Instron 4208 control panel.

2.3. Material

Hexcel's IM7/8552 carbon epoxy unidirectional tape with a nominal ply thickness of 0.125 mm was used. The material was cured in a hot plate press according to the manufacturer's specifications, which consists in submitting the material to three temperature stages: (i) 110 °C for one hour followed by (ii) 180 °C for two hours and finally (iii) cool down at 3 °C/min until room temperature. During the curing cycle, a pressure of 7 bar is applied to the material.

The IM7/8552 elastic material properties at room temperature were obtained in previous investigations [28]. Tests were also conducted to measure the elastic properties at low and high temperatures following the applicable standards [29, 30]. These moduli are required to determine the R-curve at each temperature. The tests to measure E_1 at extreme temperatures faced difficulties resulting from

debonding of the strain gauges and fracture of its connectors. This property was taken as constant since E_1 is mainly controlled by the stiffness of the fibres, which is unlikely to change substantially with temperature. Table 2 reports the elastic properties where E_1 and E_2 are respectively the longitudinal and transverse modulus, G_{12} is the shear modulus, and ν_{12} is the major Poisson's ratio.

[Table 2 about here.]

2.4. Compressive R-curve

Samples of Hexcel IM7/8552 carbon fibre composite material were cut using a diamond coated mechanical saw from a plate with a $[0/90]_{8s}$ layup and a nominal thickness of 4 mm. Notches in the samples were then machined using a vertical mill equipped with a 1 mm diameter drill bit. The crack faces separation was 1 mm. This value provides enough clearance so that the adjacent crack faces do not come in contact during compressive testing, thus invalidating the test. Also, the shape of the crack tip is unlikely to affect the value of the fracture toughness in compression where the specimens fail by kink-band formation [31].

Six different configurations were used, corresponding to references A to F (Figure 3). A total of 36 specimens were tested, 18 specimens at -50 °C and another 18 specimens at 100 °C with three samples per each configuration.

[Figure 3 about here.]

Compressive tests were carried inside the Instron 3119-007 environmental chamber under displacement control and at a speed of 0.5 mm/min. In order to use the analytical model developed by Catalanotti et al. [19], which assumes a frictionless contact between the specimen and the tool(s), a very thin layer of molybdenum disulphide (MoS_2) was applied at the specimen extremities to decrease friction (Figure 4).

[Figure 4 about here.]

2.5. Tensile R-curve

IM7/8552 material plates with $[90/0]_{8s}$ layup and nominal thickness of 4 mm were cut with a diamond-coated mechanical saw. The tensile samples were then machined in order to obtain a double notch using a vertical mill with a 1 mm drill bit. No sharp cut was performed in the crack radius of the specimens after machining the crack. It has been shown that the fracture toughness measured using a sharp crack or a 1 mm radius notch is virtually the same [32] and, at peak load, the crack may be considered sharp [33].

For the tensile tests, a total of five geometries were used labeled from A to E (Figure 5), three samples from each geometry and for each temperature were tested resulting in a total of 30 specimens, of which 15 were tested at -50 °C and another 15 were tested at 100 °C.

[Figure 5 about here.]

The Instron environment chamber was used to perform all tests at the required temperatures under displacement control at a speed of 1 mm/min. Two small pieces of a high-grit sandpaper were used at both ends of the specimens to increase the friction between the specimen and the top and bottom grips (Figure 6).

[Figure 6 about here.]

2.6. Scanning electron microscopy

The fracture surfaces of the DEN tensile specimens were examined using a FEI Quanta 400 series environment scanning electron microscope to investigate any distinct features resulting from submitting these samples to different testing temperatures. Observations were performed on the fracture surfaces of the tested samples at -50 °C and 100 °C.

3. Experiments

3.1. Experimental results for DEN compressive tests

Figure 7(a) shows one specimen from each geometry after testing at -50 °C, and Figure 7(b) shows the specimens tested at 100 °C.

[Figure 7 about here.]

Representative load vs displacement curves can be seen in Figure 8 for the specimens tested at -50 °C, and in Figure 9 for the samples tested at 100 °C. There is one curve for each of the six tested geometries at -50 °C and 100 °C. Table 3 shows the summary of the results for the two temperatures under investigation. The notation used is *C-X-0Y-Z*, where *C* represents the type of test (compression), *X* is the specimen configuration, which ranges from *A* to *F*, *Y* is the specimen number, and *Z* takes the letter *C* for -50 °C 'cold' temperature or *H* for 100 °C 'hot' temperature.

[Figure 8 about here.]

[Figure 9 about here.]

[Table 3 about here.]

3.2. Experimental results for DEN tensile tests

Figures showing the fracture surface of the specimens tested in tension can be observed in Figure 10(a). This figure shows one specimen of each tested configuration at -50 °C. Figure 10(b) shows the fractured specimens tested at 100 °C. No significant differences on the macroscopic failure surface are observed.

[Figure 10 about here.]

Figure 11 and Figure 12 depict two examples of the load vs. displacement curves. There are five curves on each graph corresponding to one of each tested configuration at -50 °C and 100 °C. Table 4 reports the results obtained experimentally for each temperature. The notation used is *T-X-0Y-Z*, where *T*

represents the type of test (tension), X is the specimen geometry which ranges from A to E, Y is the specimen number and Z represents the temperature under investigation, which is identified as C for -50 °C 'cold' temperature or H for 100 °C 'hot' temperature.

[Figure 11 about here.]

[Figure 12 about here.]

[Table 4 about here.]

4. Data analysis and discussion

4.1. Obtaining the compressive R-curve from size effect

Obtaining the R-curve of the material using the size effect method requires the knowledge of the size effect law, which dictates the relation between the nominal remote stress and the geometry of the sample i.e. $\sigma_u = \sigma_u(w)$.

The different types of regression plots described by Bažant and Planas [27] were investigated using the data obtained experimentally. Figures 13(a) and 13(b) show the experimental data and the best fitting curves for the regression methods investigated at -50 °C and 100 °C, respectively. It can be observed that the size effect law that best fits the data is the bilogarithmic for both temperatures under study with a coefficient of determination of $R^2 = 0.446$ and $R^2 = 0.4597$. The Levenberg-Marquardt algorithm implemented in Matlab [34] is used to assess the goodness of the fit. The Interval Confidence (IC) of the fitting function at 90% is calculated and reported in Figures 13(a) and 13(b). This will later allow the calculation of the Interval of Confidence for the R-curves. After the determination of the size effect law, Eq. (9) can be solved for $w = w(a)$, all the required parameters of the equation are known and can be seen in Table 5.

[Figure 13 about here.]

[Table 5 about here.]

Using Eq. (8) with the known values and with $w = w(a)$, the R-curve of the laminate, $\mathcal{R}$ is calculated. Multiplying by 2 the value of $\mathcal{R}$ for every Δa, the fracture toughness of the 0° ply ($\mathcal{R}_0$) is obtained. Figures 14 and 15 show the result of applying this methodology to obtain the R-curve at the temperatures under study. $\mathcal{R}_0$ is the envelope of the crack driving forces.

[Figure 14 about here.]

[Figure 15 about here.]

The steady-state value for the fracture toughness is obtained using the following:

$$\mathcal{R}^0_{SS} = \lim_{w \to \infty} \mathcal{R}_0 \tag{10}$$

The steady state fracture toughness value ($\mathcal{R}_{SS}$) reads 60.85 kJ/m^2 at -50 °C and 43.47 kJ/m^2 at 100 °C. The length of the fracture process zone, l_{fpz} is obtained following Bažant and Planas [27]:

$$l_{fpz} = \frac{k_0}{2k_0'} w_0 \tag{11}$$

where k_0 is $k(\alpha_0)$, k_0' is $k'(\alpha_0)$ and w_0 is the constant of Bažant size effect law, which for the bilogarithmic regression takes the value of N. The length of the fracture toughness zone, l_{fpz} is then calculated to be equal to 0.84 mm at -50 °C and 1.78 mm at 100 °C.

The compressive R-curve for IM7/8552 at the temperatures studied are shown alongside the results obtained by Catalanotti et al. [19] for the same material system (Figure 16).

[Figure 16 about here.]

4.2. Obtaining the tensile R-curve from size effect

Similar to what happened with the compressive R-curve, the relation between the nominal remote stress and the geometric parameters of the specimens used must be known ($\sigma_u = \sigma_u(w)$) to calculate the tensile R-curve.

Bažant and Planas [27] describe three approaches that were investigated to find the best fit for the tensile results at the two temperatures. Figure 17(a) and Figure 17(b) show the experimental data and the best fitting curve for the investigated methods at -50 °C and 100 °C. The law that best fits the data is the bilogarithmic for both temperatures under study with a coefficient of determination of $R^2 = 0.8404$ and $R^2 = 0.8191$, where the parameters of fitting are shown in Table 6.

[Figure 17 about here.]

[Table 6 about here.]

After determining the best size effect law for the measured data, the procedure previously described was used to obtain the tensile R-curve of the 0° ply. This is shown in Figures 18 and 19 where $\mathcal{R}_0$ is the envelope of the tensile crack driving forces.

[Figure 18 about here.]

[Figure 19 about here.]

The steady state fracture toughness value ($\mathcal{R}_{SS}$) reads 62.50 kJ/m^2 at -50 °C and 166.40 kJ/m^2 at 100 °C. The length of the fracture process zone, l_{fpz} is obtained following Bažant and Planas [27], as previously done for the compressive R-curve, which is equal to zero at -50 °C and 0.72 mm at 100 °C.

The tensile R-curve for the IM7/8552 0° ply at the extreme temperatures are shown in Figure 20. This figure includes the data obtained by Catalanotti et al. [20] at room temperature.

[Figure 20 about here.]

4.3. Discussion

The results reported in Table 2 show that the transverse modulus decreases with temperature, as indicated by a decrease from 10.61 GPa at -50 °C to

7.96 GPa at 100 °C. The same trend is observed for the shear moduli. Changing the temperature directly affects the adhesion between fibre and matrix. The key reason may lie in the different coefficient of thermal expansion of each material. The longitudinal Poisson's ratio remains almost constant throughout the temperatures considered in the study.

The tests conducted to measure the compressive fracture toughness show the scatter that is typical in compressive tests of polymer composite materials. The procedure described in Koerber et al. [35] was used to minimize not only the scatter but also the probability of premature failure of the specimen. Furthermore, previous investigations where back-to-back strain gages were used [19] indicted that the compressive test set-up was not inducing bending in the specimen. The results shown in Figure 16 indicate that, decreasing the temperature from 25 °C to -50 °C, the compressive fracture toughness does not change. However, increasing the temperature from 25 °C to 100 °C decreases the steady state fracture toughness by 29 %. The reason for this trend is likely to be related to the effects of temperature on the shear modulus of the resin and, consequently, on that of the composite ply. As shown in Table 2, the shear modulus of the ply shows a slight increase of 12 % (-50 °C). A more pronounced difference can be observed at 100 °C where the shear modulus decreases by 28 % when compared to the value measured at room temperature. Since the onset of fibre kinking depends on the shear modulus of the composite [36] any effect of temperature on the shear modulus will also affect the compressive failure of the longitudinal ply. For specimens tested in compression, that fail by kink-band formation, it can be observed (Table 3) that strength decreases with decreasing shear modulus.

Figure 20 shows that in the case of longitudinal tensile failure the maximum value of the intralaminar fracture toughness is obtained at room temperature. Increasing the temperature to 100 °C there is a decrease of 19 % on the steady-state value of the fracture toughness. A more drastic reduction of 70 % with respect to room temperature is obtained for -50 °C.

The calculated fracture process zone, using the size effect law, shows that in compression the value of l_{fpz} decreases with temperature. In compression,

l_{fpz} corresponds to the region where a kink band is broadening. This trend was observed for the range of temperatures under investigation. In tension, the value of l_{fpz} decreases if there is a decrease or increase in the temperature when compared to the same value at room temperature. This corresponds to a region where the crack is still bridged by unbroken fibres. A more ductile response is expected at 100 °C, however increasing the temperature modifies the residual stress field at the fibre-matrix interface, due to the difference values of each respective coefficient of temperature expansion, and thus modifying the process of crack propagation.

The exact mechanisms that justify these observations need to be studied in detail, possibly with the use of computational micromechanics. In any case, it is apparent that the effect of temperature on the properties of the fibre-matrix interface and on the local stress fields influence both the fracture toughness and the length of the fracture process zone to a point where a quite brittle response is obtained at -50 °C.

4.4. SEM observations of the tensile specimens

Typical fracture surfaces at -50 °C and 100 °C are shown in Figures 21 and 22, respectively. There is a remarkable difference between the fracture surfaces. The fracture surface at the lowest temperature is practically perpendicular to the direction of the applied load with a very clean cleavage fracture plane indicating a more brittle failure mode. At 100 °C, the fracture surface presents irregular fragmented breaks in which some areas have bundles of fibres without any supporting matrix. This is an indication of a more ductile fracture.

[Figure 21 about here.]

[Figure 22 about here.]

5. Conclusions

The method proposed to measure the fracture toughness of polymer composites does not require any post processing or tracking of the crack position

during test. Therefore, the present method offers an advantage over alternative methods. The experiments can be performed without good visibility of the test specimen and crack tip position.

For the material used here, it was observed that some material properties are insensitive to the change in temperature (for the temperatures under investigation), such as the longitudinal Poisson's ratio. The longitudinal modulus was kept constant for all studied temperatures this is due to the challenges faced to measure this property under extreme temperature conditions. E_1 is mainly controlled by the stiffness of the fibres and is unlikely to change in the range of temperatures considered in the present study.

The transverse and shear modulus decrease when the temperature increases. E_2 decreases 14 % between -50 °C and room temperature and another 12 % when the temperature goes up to 100 °C. The shear modulus decreases 11 % from -50 °C to room temperature but the highest drop in value is observed when G_{12} is evaluated between RT and 100 °C where the value drops from 5.29 GPa to 3.83 GPa, which corresponds to a drop of 28 %. It is concluded that the temperature plays an important role in the fracture toughness of the composite material under investigation. By measuring the full R-curve, it is not only possible to assess the steady state value of the fracture toughness but also the length of the fracture process zone and their respective variations with temperature. Under compression, the steady state fracture toughness value does not change with the decreased in temperature to -50 °C but there is a decrease to 43.47 kJ/m^2 when the temperature is increased to 100 °C, which represents a 29 % decrease when compared to the $\mathcal{R}_{SS}$ at room temperature. The fracture process zone decreases as the temperature decreases first by 24 % between 100 °C and room temperature, and then by 41 % between room temperature and -50 °C. In compression, where failure is by kink-band formation, the fracture process zone l_{fpz} corresponds to the region where the kink-band is broadening.

The maximum value of the tensile steady-state fracture toughness is obtained at room temperature ($\mathcal{R}_{SS}^{RT}$=205.31 kJ/m^2). The steady-state value of the tensile fracture toughness decreases when the temperature is increased to 100 °C

or decreased to -50 °C taking the values of 166.40 kJ/m^2 and 62.50 kJ/m^2, respectively. The fracture process zone follows the same trend where the highest value is measured at room temperature and equals 2.63 mm. The length of the fracture process zone reduces rapidly when compared to the value obtained at 100 °C (73 % reduction). There is a drastic drop when looking at the result measured at -50 °C, where the length of the fracture process zone is equal to zero. In tension, l_{fpz} corresponds to a region where there is bridging by unbroken fibres.

The SEM observations indicate that at cryogenic temperatures there is a brittle fracture where the fracture surface is perpendicular to the applied load direction and the surface itself has a constant topology. At high temperatures the fracture surface shows loose bundles of fibres without any supporting material. This is due to the softening of the matrix with the increase in temperature and subsequent decohesion events that take place in the interface between fibre and matrix.

Future work will attempt to further understand the observed trends by developing appropriate thermo-mechanical computational models developed at the micro-scale.

6. Acknowledgements

The present work was supported by the SHEFAE European project, FP7-AAT-2012-RTD-JAPAN, Grant agreement no. 314307.

References

[1] P. P. Camanho, M. A. Bessa, G. Catalanotti, M. Vogler, R. Rolfes, Modeling the inelastic deformation and fracture of polymer composites – Part II: Smeared crack model, Mechanics of Materials 59 (2013) 36–49.

[2] C. Schuecker, H. E. Pettermann, A continuum damage model for fiber reinforced laminates based on ply failure mechanisms, Composite Structures 76 (1–2) (2006) 162–173.

[3] P. Camanho, G. Erçin, G. Catalanotti, S. Mahdi, P. Linde, A finite fracture mechanics model for the prediction of the open-hole strength of composite laminates, Composites Part A: Applied Science and Manufacturing 43 (8) (2012) 1219–1225.

[4] E. Abisset, F. Daghia, P. Ladevèze, On the validation of a damage mesomodel for laminated composites by means of open-hole tensile tests on quasi-isotropic laminates, Composites Part A: Applied Science and Manufacturing 42 (10) (2011) 1515–1524.

[5] M. Vogler, R. Rolfes, P. Camanho, Modeling the inelastic deformation and fracture of polymer composites – Part I: Plasticity model, Mechanics of Materials 59 (2013) 50–64.

[6] S. Pinho, P. Robinson, L. Iannucci, Fracture toughness of the tensile and compressive fibre failure modes in laminated composites, Composites Science and Technology 66 (13) (2006) 2069–2079.

[7] G. Catalanotti, P. Camanho, J. Xavier, C. Dávila, A. Marques, Measurement of resistance curves in the longitudinal failure of composites using digital image correlation, Composites Science and Technology 70 (13) (2010) 1986–1993.

[8] A. K. Kaw, Mechanics of composite materials, Taylor & Francis, Boca Raton, FL, 2006.

[9] I. M. Ward, Mechanical properties of solid polymers, John Wiley & Sons, London, 1971.

[10] J. D. Ferry, Viscoelastic properties of polymers, John Wiley & Sons, London, 1980.

[11] R. Adams, M. Singh, Low temperature transitions in fibre reinforced polymers, Composites Part A: Applied Science and Manufacturing Composites Part A: Applied Science and Manufacturing 32 (6) (2001) 797–814.

[12] K. Reifsnider, S. Case, J. Duthoit, The mechanics of composite strength evolution, Composites science and technology. 60 (12-13) (2000) 2539–2546.

[13] C. A. Mahieux, B. E. Russell, K. L. Reifsnider, Stress Rupture of Unidirectional High Performance Thermoplastic Composites in End-Loaded Bending at Elevated Temperatures. Part I: Experimental Characterization of the Failure Mode, Journal of Composite Materials 32 (14) (1998) 1311–1321.

[14] B. M. Walther, An investigation of the tensile strength and stiffness of unidirectional polymer-matrix, carbon-fiber composites under the influence of elevated temperatures, University Libraries, Virginia Polytechnic Institute and State University, Blacksburg, Va., 1998.

[15] K. Whitley, T. Gates, Thermal/Mechanical Response and Damage Growth in Polymeric Composites at Cryogenic Temperatures, in: 43rd AIAA/ASME/ASCE/AHS/ASC Structures, Structural Dynamics, and Materials Conference, American Institute of Aeronautics and Astronautics, 2002.

[16] H. S. Kim, W. X. Wang, Y. Takao, Effects of temperature and fiber orientation on the mode I interlaminar fracture toughness of carbon/epoxy composites, ICCM-12 paper 276.

[17] H. S. Kim, W. X. Wang, Y. Takao, Effects of temperature and fiber orientation on mode II interlaminar fracture behavior of carbon/epoxy composites, Durability of composite systems, Myano, Cardon, Reifsnider, Fukuda and Ogihara (Eds), Balkema, Lisse (2001) 377–383.

[18] M. J. Laffan, S. T. Pinho, P. Robinson, A. J. McMillan, Translaminar fracture toughness testing of composites: A review, Polymer Testing 31 (3) (2012) 481–489.

[19] G. Catalanotti, J. Xavier, P. P. Camanho, Measurement of the compressive

crack resistance curve of composites using the size effect law, Composites Part A: Applied Science and Manufacturing 56 (2014) 300–307.

[20] G. Catalanotti, A. Arteiro, M. Hayati, P. P. Camanho, Determination of the mode I crack resistance curve of polymer composites using the size-effect law, Engineering Fracture Mechanics 118 (2014) 49–65.

[21] Z. P. Bažant, J. J. H. Kim, I. M. Daniel, E. Becq-Giraudon, G. Zi, Size effect on compression strength of fiber composites failing by kink band propagation, in: Z. P. Bažant, Y. D. S. Rajapakse (Eds.), Fracture Scaling, Springer Netherlands, 1999, pp. 103–141, dOI: 10.1007/978-94-011-4659-3_7.

[22] P. M. Moran, X. H. Liu, C. F. Shih, Kink band formation and band broadening in fiber composites under compressive loading, Acta Metallurgica et Materialia 43 (8) (1995) 2943–2958.

[23] Z. P. Bažant, J. Planas, Fracture mechanics and size effect: concrete and other quasibrittle materials, CRC Press, Boca Raton, FL, 1997.

[24] G. Catalanotti, J. Xavier, Measurement of the mode {II} intralaminar fracture toughness and r-curve of polymer composites using a modified iosipescu specimen and the size effect law, Engineering Fracture Mechanics 138 (2015) 202 – 214.

[25] Z. Suo, G. Bao, B. Fan, T. Wang, Orthotropy rescaling and implications for fracture in composites, SAS International Journal of Solids and Structures 28 (2) (1991) 235–248.

[26] G. Bao, S. Ho, Z. Suo, B. Fan, The role of material orthotropy in fracture specimens for composites, International Journal of Solids and Structures 29 (9) (1992) 1105–1116.

[27] Z. P. Bažant, J. Planas, Fracture and size effect in concrete and other quasibrittle materials, CRC Press, Boca Raton [etc.], 1997.

[28] P. P. Camanho, P. Maimí, C. G. Dávila, Prediction of size effects in notched laminates using continuum damage mechanics, Composites Science and Technology 67 (13) (2007) 2715–2727.

[29] ASTM D3039 / D3039 M - 00 Standard Test Method for Tensile Properties of Polymer Matrix Composite Materials.

[30] ASTM D3518 / D3518 M - 01 Standard Test Method for In-Plane Shear Response of Polymer Matrix Composite Materials by Tensile Test of a 45 Laminate.

[31] W. Jackson, J. Ratcliffe, Measurement of fracture energy for kink-band growth in sandwich specimens, Proceedings of the 2nd international conference on composites testing and model identification, Comptest 2004, University of Bristol, Bristol, UK.

[32] P. P. Camanho, G. Catalanotti, On the relation between the mode I fracture toughness of a composite laminate and that of a 0 ply: Analytical model and experimental validation, Engineering Fracture Mechanics 78 (13) (2011) 2535–2546.

[33] R. M. Foote, Y.-W. Mai, B. Cotterell, Crack growth resistance curves in strain-softening materials, Journal of the Mechanics and Physics of Solids Journal of the Mechanics and Physics of Solids 34 (6) (1986) 593–607.

[34] MATLAB, version 7.10.0 (R2016a), The MathWorks Inc., Natick, Massachusetts, 2016.

[35] H. Koerber, J. Xavier, P. P. Camanho, High strain rate characterisation of unidirectional carbon-epoxy IM7-8552 in transverse compression and in-plane shear using digital image correlation, Mechanics of Materials 42 (11) (2010) 1004–1019.

[36] C. Dávila, P. Camanho, C. Rose, Failure criteria for FRP laminates, Journal of Composite Materials 39 (4) (2005) 323–345.

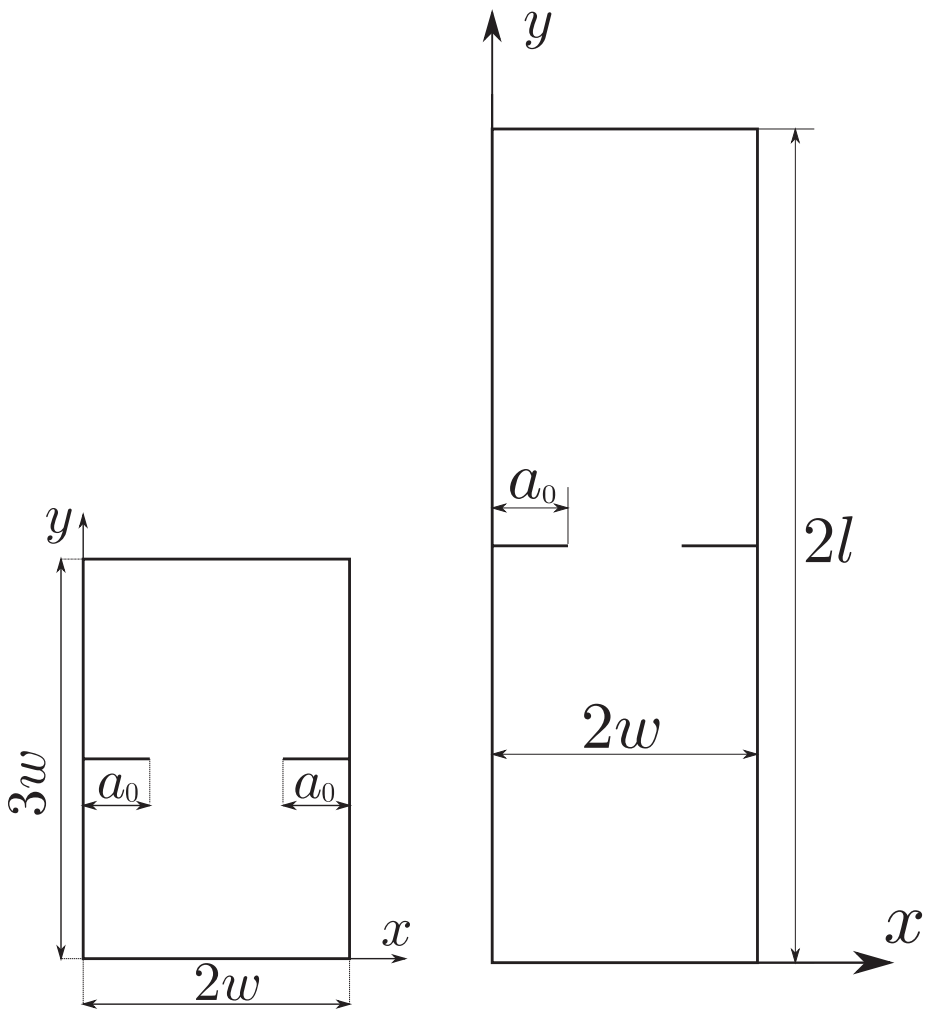

Figure 1: Double edge notched compression specimen (left) [19] and double edge notched tension specimen (right) [20].

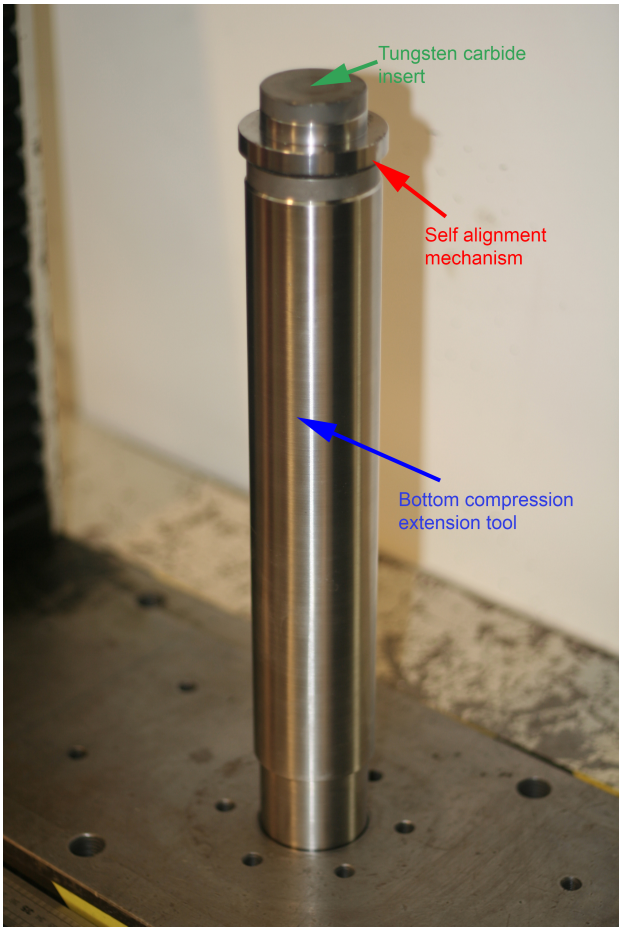

Figure 2: Bottom portion of the compressive testing rig showing the extension coupled with the self alignment mechanism.

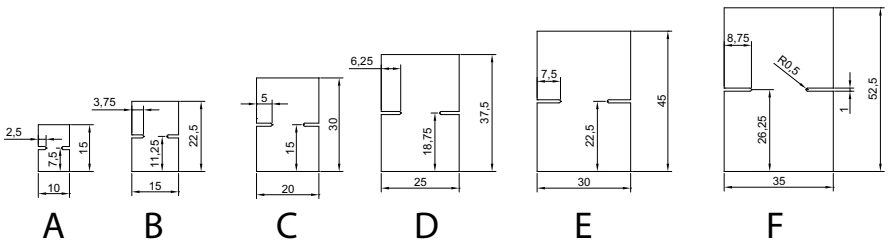

Figure 3: Compression specimen geometries showing dimensions from A to F in mm [19].

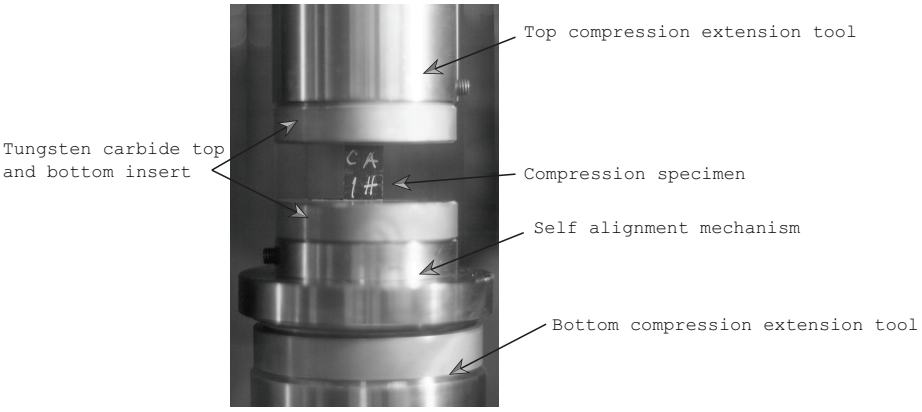

Figure 4: Compression specimen #1 from set A undergoing test at 100°C.

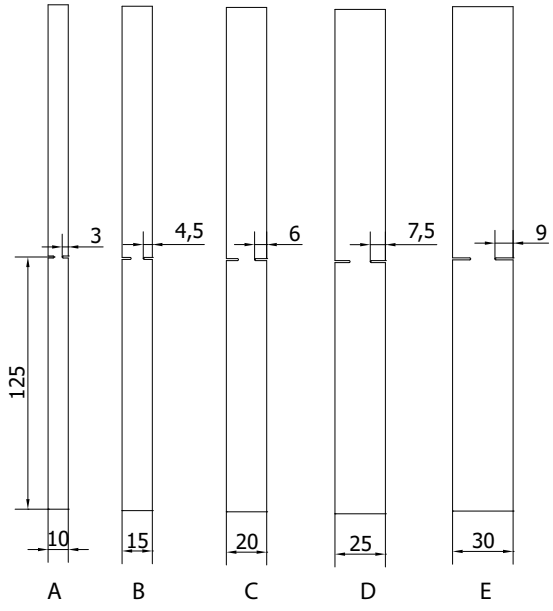

Figure 5: Tensile specimen geometries showing dimensions from A to E in mm.

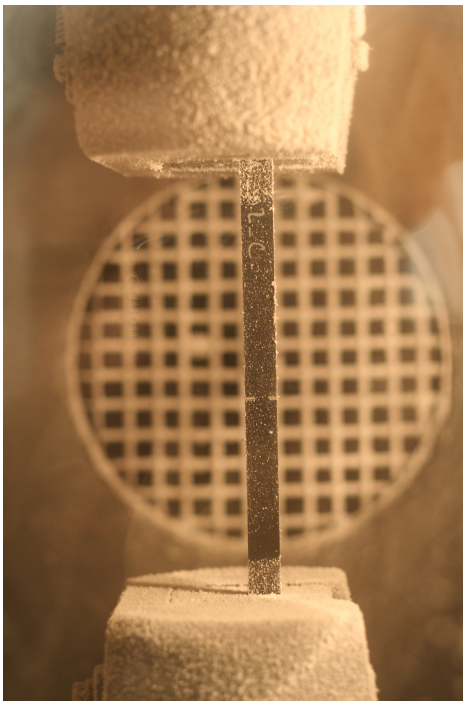

Figure 6: Geometry A tensile specimen #2 undergoing testing at $-50°C$.

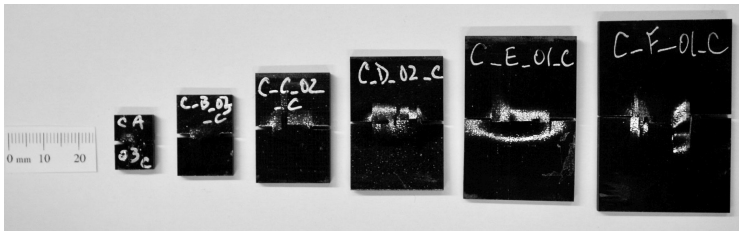

(a)

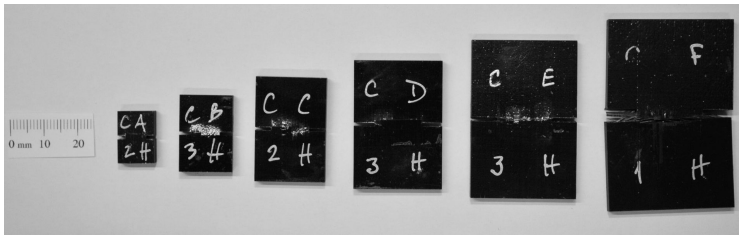

(b)

Figure 7: Compression specimens after testing at (a) $-50°$C and (b) $100°$C.

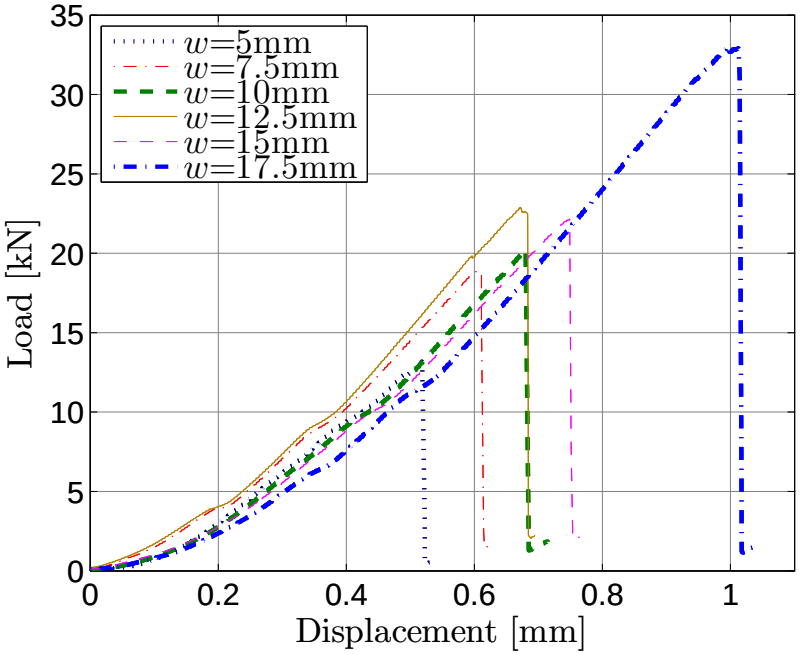

Figure 8: Load vs displacement curves for compression tests at $-50°$C.

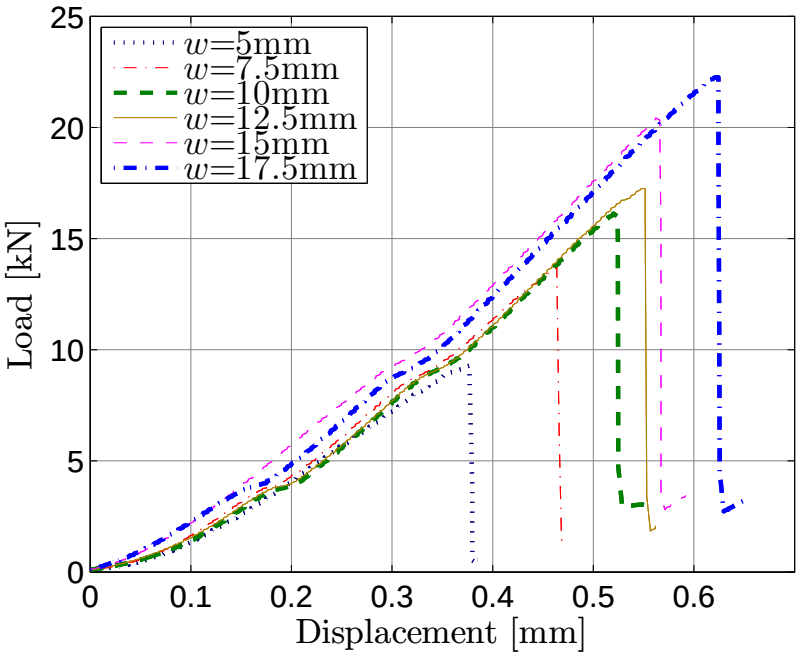

Figure 9: Load vs displacement curves for compression tests at 100°C.

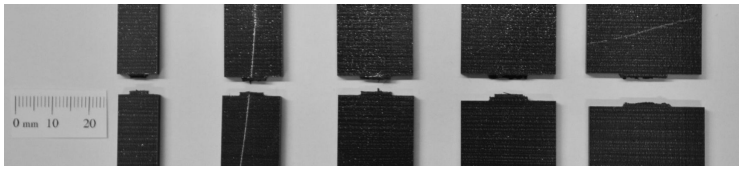

(a)

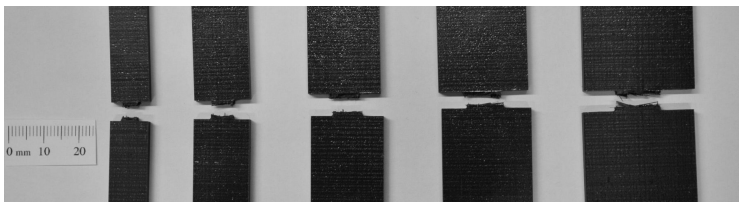

(b)

Figure 10: Tension specimens after testing at (a) −50°C and (b) 100°C.

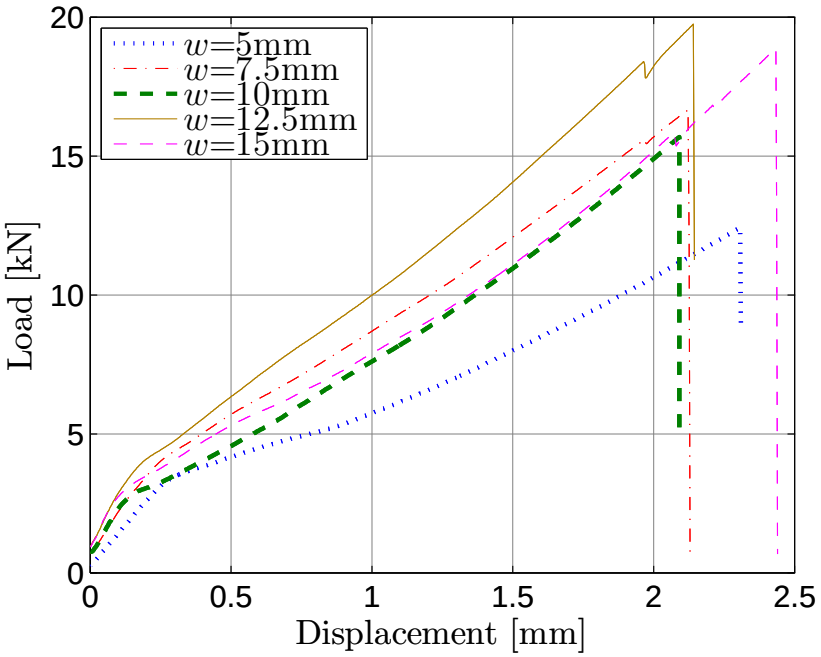

Figure 11: Load vs displacement curves for tension tests at $-50°$C.

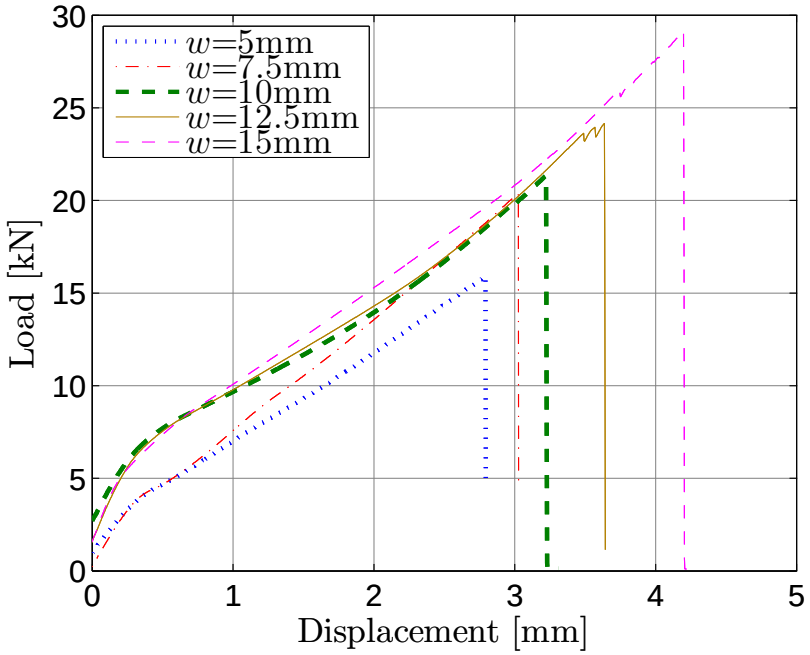

Figure 12: Load vs displacement curves for tension tests at 100°C.

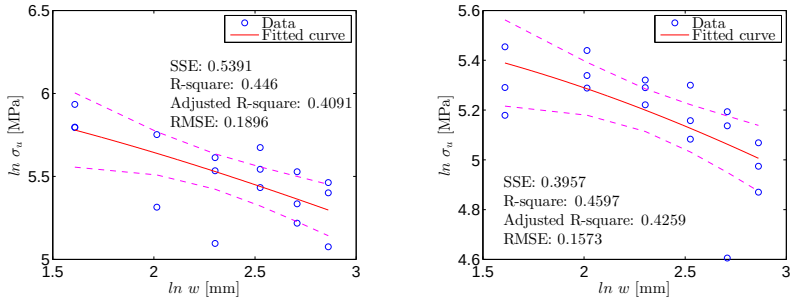

Figure 13: Size effect law and best fitting for compressive tests at (a) −50°C and (b) 100°C.

550

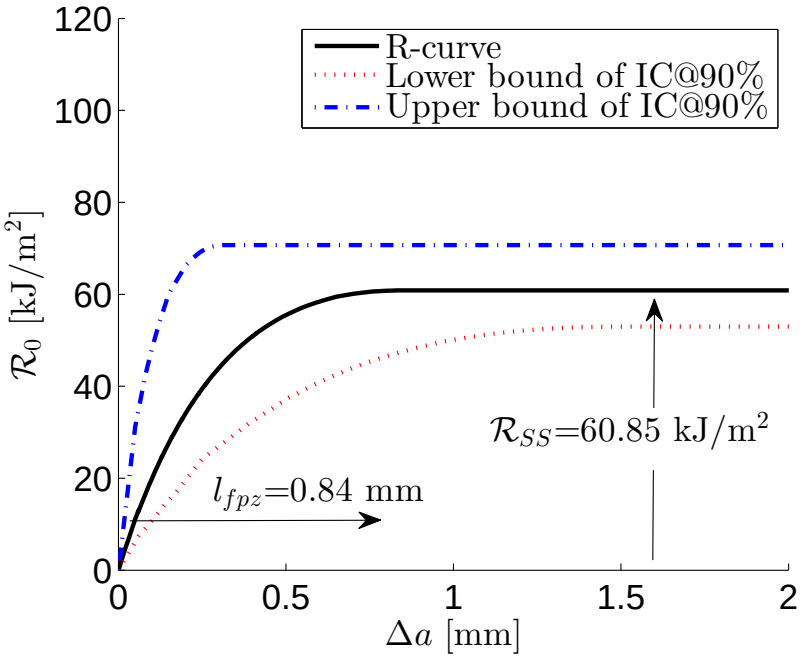

Figure 14: Envelope of the compressive crack driving force curves and R-curve for IM7/8552 at $-50°C$.

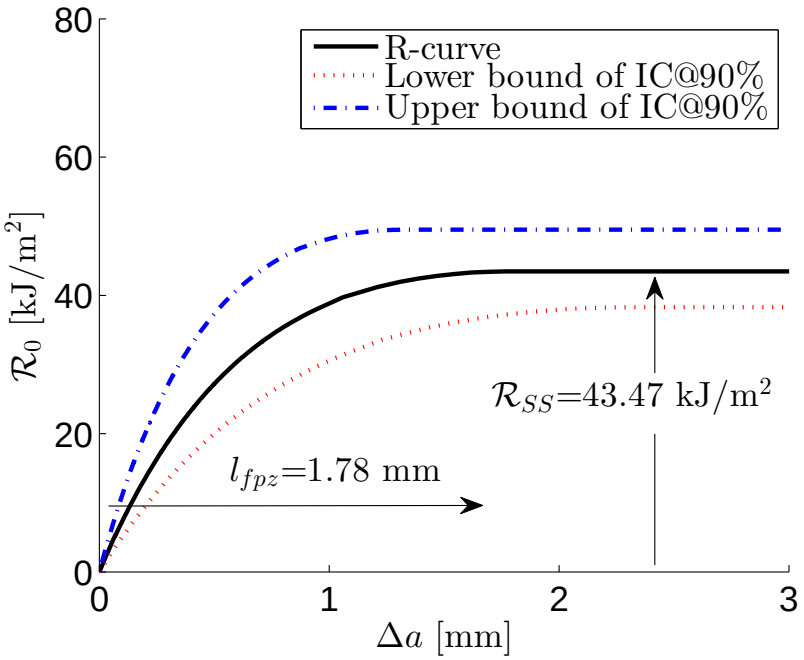

Figure 15: Envelope of the compressive crack driving force curves and R-curve for IM7/8552 at 100°C.

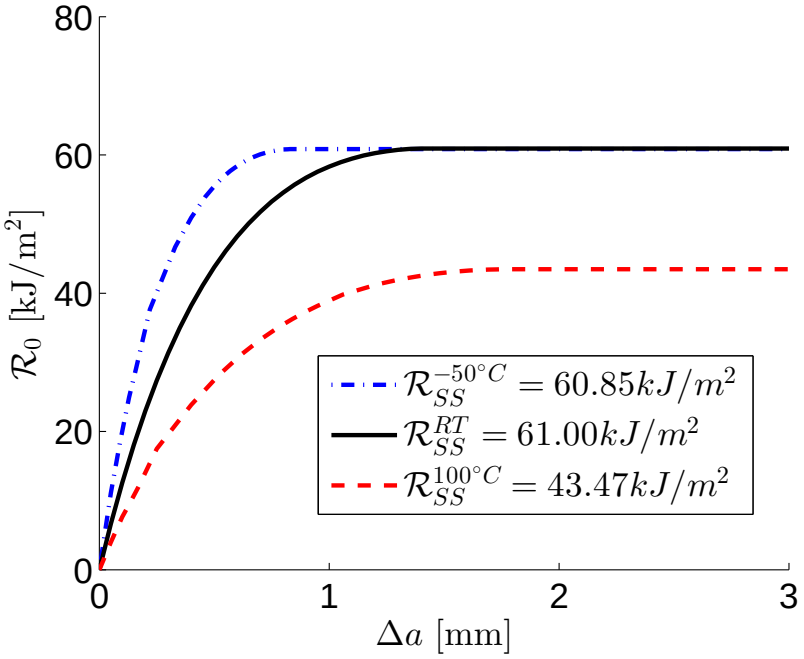

Figure 16: Compressive R-curve for IM7/8552 at $-50°C$, room temperature [19] and $100°C$.

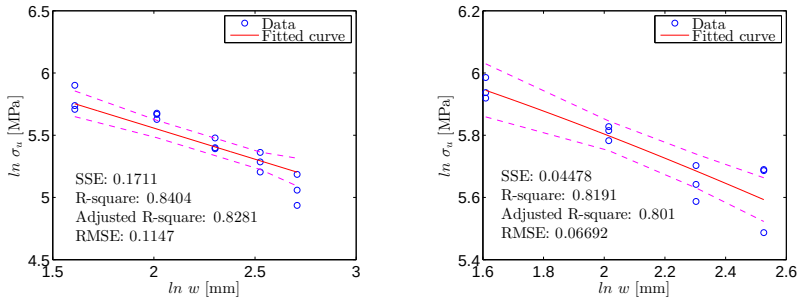

Figure 17: Size effect law and best fitting for tensile tests at (a) $-50°$C and (b) $100°$C.

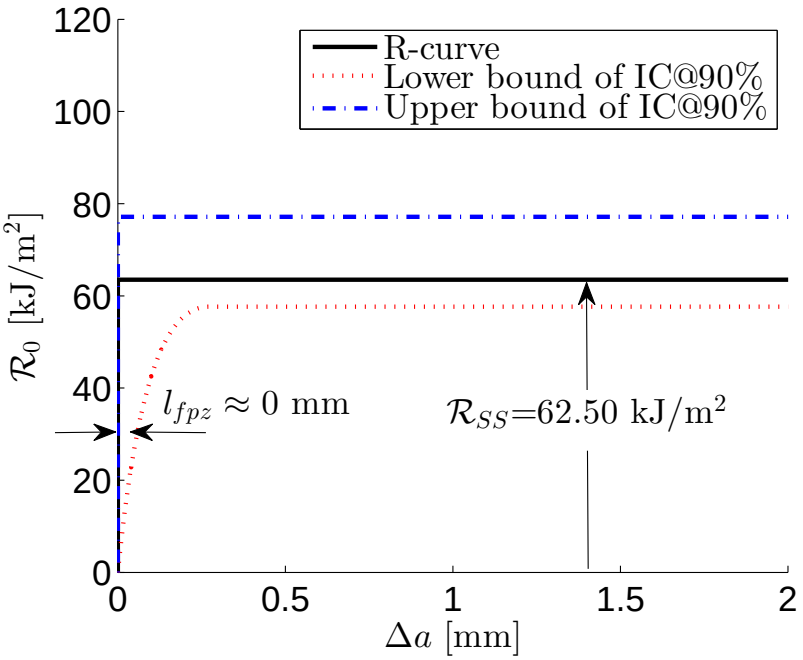

Figure 18: Envelope of the tensile crack driving force curves and R-curve for IM7/8552 at $-50°$C.

555

560

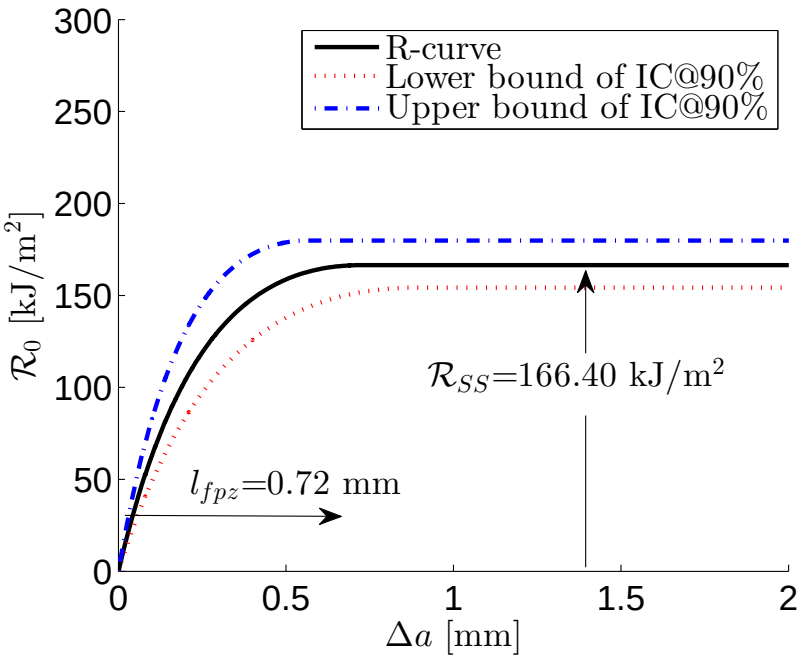

Figure 19: Envelope of the tensile crack driving force curves and R-curve for IM7/8552 at 100°C.

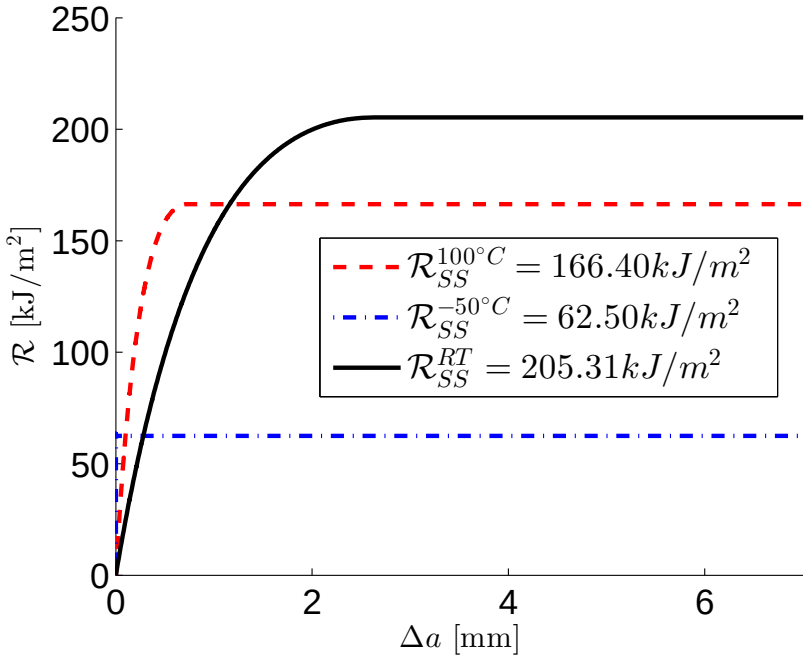

Figure 20: Tensile R-curve for IM7/8552 at −50°C, room temperature [20] and 100°C.

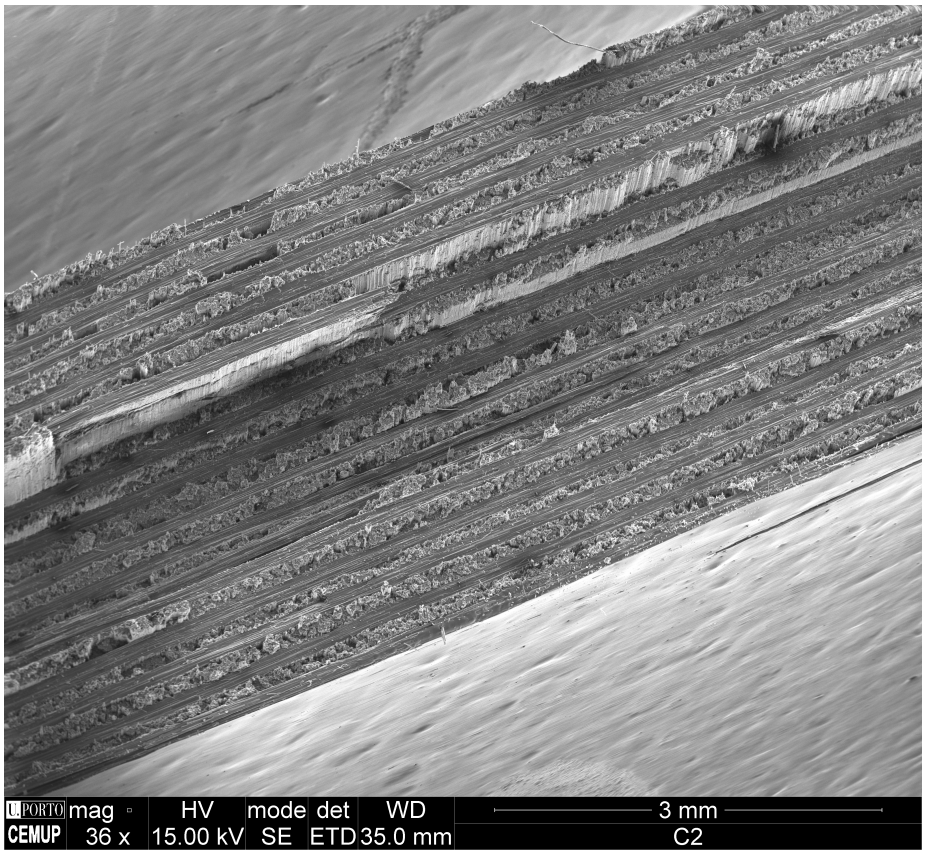

Figure 21: SEM fracture surface for DEN tensile specimen tested at $-50°$C.

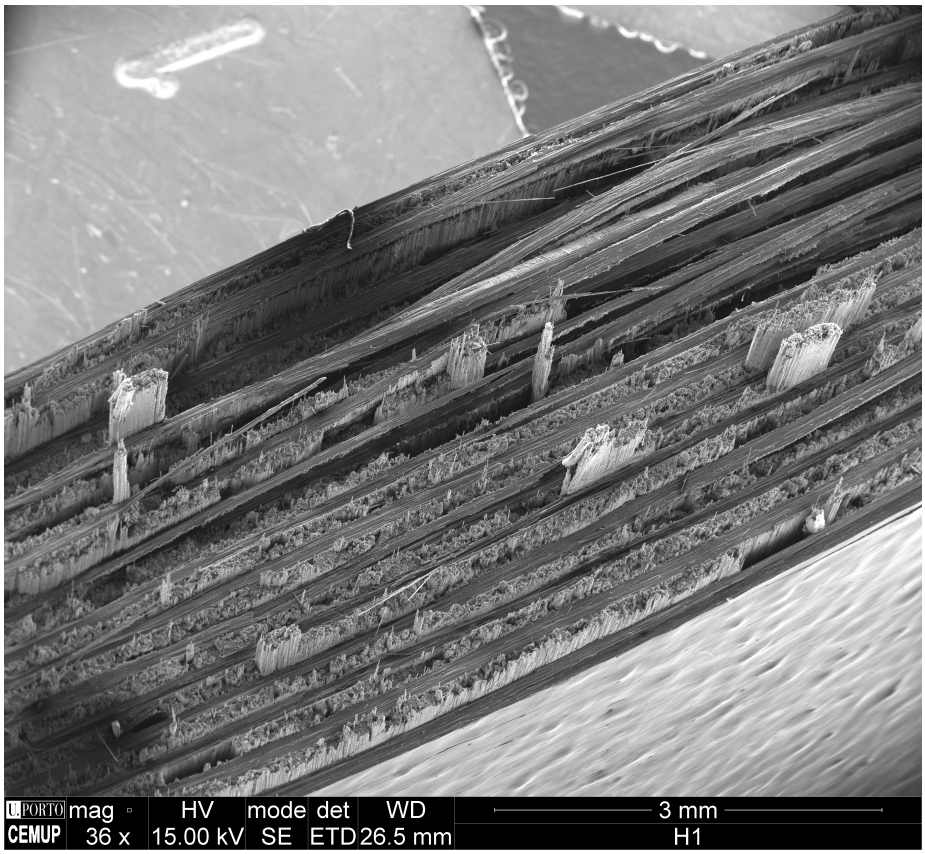

Figure 22: SEM fracture surface for DEN tensile specimen tested at 100°C.

Regression fit	Formula	Fitting parameters	R_{SS}	l_{fpz}
Bilogarithmic	$\ln \sigma_u = \ln \frac{M}{\sqrt{N+w}}$	M, N	$\frac{k_0^2}{E} M^2$	$\frac{k_0}{2\acute{k}_0} N$
Linear regression I	$\frac{1}{\sigma_u^2} = Aw + C$	A, C	$\frac{k_0^2}{E} \frac{1}{A}$	$\frac{k_0}{2\acute{k}_0} \frac{C}{A}$
Linear regression II	$\frac{1}{w\sigma_u^2} = \acute{A} \frac{1}{w} + \acute{C}$	$\acute{A}, \acute{C}$	$\frac{k_0^2}{E} \frac{1}{\acute{C}}$	$\frac{k_0}{2\acute{k}_0} \frac{\acute{A}}{\acute{C}}$

Table 1: Size–effect laws and fitting parameters [27].

Temperature $[^\circ C]$	E_1 [GPa]	E_2 [GPa]	G_{12} [GPa]	ν_{12}
-50	-	10.61	5.92	0.3287
RT [28]	171.42	9.08	5.29	0.32
100	-	7.96	3.83	0.3259
Standard	-	Ref. [29]	Ref. [30]	Ref. [29]

Table 2: IM7/8552 elastic properties at $-50°$C, room temperature and $100°$C.

Sample geometry	A	B	C	D	E	F
$2w$ $[mm]$	10	15	20	25	30	35
Area $[mm^2]$	40	60	80	100	120	140
$\bar{\sigma_u}^{-50^\circ C}$ [MPa]	345.17	259.10	230.18	258.48	214.62	205.90
STDV ($\sigma_u^{-50^\circ C}$) [MPa]	23.01	55.77	47.98	25.58	27.88	32.86
$\bar{\sigma_u}^{100^\circ C}$ [MPa]	201.63	210.47	194.58	177.67	150.07	144.64
STDV ($\sigma_u^{100^\circ C}$) [MPa]	23.28	13.40	8.05	15.86	35.61	11.69

Table 3: Summary of the compressive experimental results at $-50^\circ C$ and $100^\circ C$.

565

Sample geometry	A	B	C	D	E
$2w$ $[mm]$	10	15	20	25	30
Area $[mm^2]$	40	60	80	100	120
$\bar{\sigma_u}^{-50^\circ C}$ [MPa]	325.80	286.40	226.72	197.56	158.38
STDV ($\sigma_u^{-50^\circ C}$) [MPa]	28.33	6.18	8.96	12.70	16.07
$\bar{\sigma_u}^{100^\circ C}$ [MPa]	382.87	333.13	282.85	277.35	222.70
STDV ($\sigma_u^{100^\circ C}$) [MPa]	10.76	6.28	13.34	25.34	14.62

Table 4: Summary of the tensile experimental results at -50°C and 100°C.

Temperature $[^\circ C]$	M [MPa$\sqrt{\text{mm}}$]	N [MPa$\sqrt{\text{mm}}$]	E [MPa]	α_0	ρ
-50	898.30	2.71	91491	0.6	7.69
100	721.90	5.87	90056	0.6	11.73

Table 5: Summary of the required parameters to determine the R-curve in compression at -50 °C and 100 °C.

Temperature $[^\circ C]$	M [MPa$\sqrt{\text{mm}}$]	N [MPa$\sqrt{\text{mm}}$]	E [MPa]	α_0	ρ
-50	704.40	≈ 0	91491	0.6	7.69
100	1035.00	2.36	90056	0.6	11.73

Table 6: Summary of the required parameters to determine the R-curve in tension at -50 °C and 100 °C.